energies

MDPI

Article

Easy and Scalable Syntheses of $Li_{1.2}Ni_{0.2}Mn_{0.6}O_2$

Pier Paolo Prosini *, Annalisa Aurora, Livia Della Seta and Claudia Paoletti

ENEA—Research Center Casaccia, Via Anguillarese 301, 00123 Rome, Italy; annalisa.aurora@enea.it (A.A.); livia.dellaseta@enea.it (L.D.S.); claudia.paoletti@enea.it (C.P.)

* Correspondence: pierpaolo.prosini@enea.it

Abstract: Solid-state and sol-gel syntheses were selected as easy and scalable methods to prepare a lithium-rich cathode material for lithium-ion batteries. Among the extended family of layered oxides, $Li_{1.2}Ni_{0.2}Mn_{0.6}O_2$ was chosen for its low nickel content and the absence of cobalt. Both synthesis methods involved two heating steps at different temperatures, 600 and 900 °C. The first step is needed to decompose the metal acetates, which were selected as precursors, and the second step is needed to crystallise the material. To obtain a material with well-defined defects, the rate of heating and cooling was carefully controlled. The materials were characterised by X-ray diffraction, SEM coupled with EDS analysis, and thermal analysis and were finally tested as cathodes in a lithium semi cell. The solid-state synthesis allowed us to obtain better structural characteristics with respect to the sol-gel one in terms of a well-formed hexagonal layer structure and a reduced Li^+/Ni^{2+} disorder. On the other hand, the sol-gel method produced a material with a higher specific capacity. The performance of this latter material was then evaluated as a function of the discharge current, highlighting its good rate capabilities.

Keywords: Li-rich compounds; chemical synthesis; electrochemical properties

check for updates

Citation: Prosini, P.P.; Aurora, A.; Della Seta, L.; Paoletti, C. Easy and Scalable Syntheses of $Li_{1.2}Ni_{0.2}Mn_{0.6}O_2$. *Energies* **2023**, *16*, 7674. https://doi.org/10.3390/en16227674

Academic Editor: Bartłomiej Igliński

Received: 17 October 2023
Revised: 10 November 2023
Accepted: 16 November 2023
Published: 20 November 2023

1. Introduction

Storage systems are critical to the future of renewable energy, as they are essential for managing hourly and seasonal variations in renewable electricity production. Batteries are the most scalable type of grid-scale storage, and the market has seen strong growth in recent years. Thanks to their high energy density, lithium-ion batteries have found wide application as renewable energy storage systems. However, the high cost of these batteries represents an obstacle to their extensive use. The development of new materials and cutting-edge technological solutions is necessary to further increase the use of lithium-ion batteries. To make the use of lithium batteries economically advantageous, it is necessary to find new materials with high capacity and low-cost production methods.

Lithium-rich layered oxides with the chemical formula xLi_2MnO_3 $(1-x)$ $LiMO_2$ (M = Mn, Ni, and Co) are considered materials of choice to be used as cathodes for next-generation Li-ion batteries [1]. The early work by Lu et al. [2] demonstrated the stable reversible capacity of the series $Li_{4/3-2x/3}Ni_xMn_{2/3-x/3}O_2$, in which $Li_{1.11}Ni_{0.33}Mn_{0.56}O_2$ (x = 0.33) exhibited a specific capacity of ~230 mAh g^{-1}. Starting from this composition, it was observed that the increase in the Ni/Mn ratio improved the rate performance and suppressed the potential shift during cycling. However, it decreased the discharge capacity at low C-rate [3]. The Li/(Ni + Mn) ratio was controlled to increase the discharge capacity for a high-Ni/Mn-ratio cathode ($Li_{1.2}Ni_{0.35}Mn_{0.45}O_2$). The decrease in the Li/(Ni + Mn) ratio from 1.2/0.8 ($Li_{1.2}Ni_{0.35}Mn_{0.45}O_2$) to 1.16/0.84 ($Li_{1.16}Ni_{0.37}Mn_{0.47}O_2$) was effective in increasing the discharge capacity without harming the high rate performance and small potential shift [4]. Among various compositions, $Li_{1.5}Ni_{0.25}Mn_{0.75}O_{2.5}$ ($Li_{1.2}Ni_{0.2}Mn_{0.6}O_2$ or $0.5Li_2MnO_3$ $0.5LiNi_{0.5}Mn_{0.5}O_2$ in layered notation) has attracted much interest because it is also considered to be an intergrown composite [5]. $Li_{1.5}Ni_{0.25}Mn_{0.75}O_{2.5}$ (LNMO) has low nickel content and it is cobalt-free, making it environmentally friendly [6].

From a practical point of view, LNMO exhibits a low capacitance at a high discharge rate, a low Coulomb efficiency of the first cycle, and a constant loss of capacitance and voltage decrease during the charge–discharge process [7]. Several strategies have been explored to overcome these limits, including surface coating and doping with other cations or anions. Surface coating was carried out by adding, during the synthesis, metal fluorides such as CoF_2 [8], and MnF_2 [9] or metal oxides including MnO_2 [10], WO_3 [11], SiO_2 [12], and Al_2O_3 [13]. Solid ion-conducting materials such as Li_3VO_4 [14], $Li_4Ti_5O_{12}$ [15], $LiAlO_2$ [16], and Li_3PO_4 [17] have also been used. The use of the specific doping ions Cr [18], Mg [19], Zr [20], Na [21], K [22], and Nd [23] can increase the specific capacity and improve the cyclability of LNMO; on the other hand, the available capacity of the cathode materials can be reduced using dopants [24] or electrochemically inactive coating agents [25].

Another method to improve the characteristics of LNMO without penalising its specific capacity is to introduce defects into the structure of the material [26] by changing the synthesis process. In fact, the different synthesis methods can lead to the formation of different morphologies that, in turn, can modify the stability of the structure and improve its electrochemical performance. Li-rich layered compounds with different morphologies can be prepared through a wide variety of synthesis routes including solid-state [27], molten-salt [28], solvothermal [29], sol-gel [30], combustion-process [31], ball-milling [32], sol-freeze-drying [33], hydrothermal [34], microwave-heating-process [35], templating-process [36], lithium-ion-exchange-reaction [37], and aqueous-coprecipitation [38] methods. In their work, Cai et al. argue that introducing defects via a high-temperature solid-state reaction followed by a well-defined cooling process is an easy way to create high-performance LNMOs [26]. Seeking an easy method for LNMO synthesis which does not involve the use of doping agents, we focused on solid-state synthesis and on the modified Pechini method, which represent the most-used methods for the preparation of electrode materials [39]. Furthermore, to ensure good reproducibility of the high-temperature reaction, we precisely fixed the heating and cooling rates. This also allowed us to manage defects that were created within the material in a controlled way. The solid-state method has the advantage of being a very simple procedure, consisting of a precursor weighing phase and a subsequent mixing phase. In such a way, it is easy to obtain the correct stoichiometry. However, it must be considered that during the synthesis, the various metal ions must diffuse within the phase being formed, overcoming micrometre distances. The different diffusivities of the metal ions can lead to a nonuniform distribution of the various elements within the synthesised material. Therefore, a solid-state synthesis is not a homogeneous phase reaction, especially when large numbers of metal ions participate together in the reaction. Solution-based synthesis (such as coprecipitation or aqueous sol-gel) are more viable or feasible as they can provide atomic-level mixing of transition metal ions and hence homogeneity in the final material. Jarvis et al. [40] showed that these two routes, sol-gel and coprecipitation, do not affect the structure of LNMO materials. Among the sol-gel methods, the most popular is the Pechini method, described in a 1967 patent [41]. Thanks to the use of some alpha-hydroxycarboxylic acids, such as citric, lactic, and glycolic acids, it was possible to form chelates of polybasic acid with different cations. The chelates underwent polyesterification by heating in the presence of a polyhydric alcohol (i.e., ethylene glycol) to transform them into a solid resin. This resin was able to maintain a homogeneous distribution of cations during the high-temperature step. In the following years, this method was modified, with the ethylene glycol being replaced with water, which gives rise to an amorphous, gelatinous matter instead of the polymer. This process, called the modified Pechini method, has become one of the most popular synthesis methods for the synthesis of complex oxide materials due to its simplicity and versatility. To compare the effect of these two synthetic methods on the material electrochemical properties, in the present work, two LNMOs obtained by reaction in the solid state or by the sol-gel method were prepared, characterised, and electrochemically tested.

2. Materials and Methods

Solid-state preparation of $Li_{1.2}Mn_{0.6}Ni_{0.2}O_2$: First, 3.06 g of lithium acetate dihydrate (Sigma–Aldrich, St. Louis, MI, USA, for synthesis 99%, MW = 102.03, 0.030 mol), 1.244 g of nickel acetate tetrahydrate (Sigma–Aldrich, purum > 99%, MW = 248.84, 0.005 mol), and 3.676 g of manganese acetate tetrahydrate (Sigma–Aldrich, for synthesis 99%, MW = 245.09, 0.015 mol) were weighed and transferred to a mortar. The amount of the three reactants was calculated stoichiometrically according to the chemical formula $Li_{1.2}Mn_{0.6}Ni_{0.2}O_2$. The powders were mixed by hand, placed in a muffle furnace, and heated under air atmosphere at a rate of 1 °C per minute up to 600 °C. The mixture was maintained at this temperature for 8 h to allow acetate decomposition and then cooled at a rate of 8 °C per minute. After cooling, the mixture was mixed again and heated at a rate of 1 °C per minute until it reached 900 °C. The material was left at this temperature for 7 h and then cooled at a rate of 8 °C per minute.

Sol-gel preparation of $Li_{1.2}Mn_{0.6}Ni_{0.2}O_2$: Stoichiometric amounts of the acetates, as previously reported, were weighed and dissolved in 50 mL of water containing 9.6 g of citric acid (Sigma–Aldrich, ACS reagent $\geq$ 99.5%, MW = 192.12, 0.05 mol, molar ratio Li+Mn+Ni: citric acid = 1:1). The solution was heated to 80 °C to facilitate the dissolution of the salts. Then the temperature was raised to 100 °C to favour water evaporation. The dry solid was mixed by hand and placed in a muffle furnace following the previous heating treatment: a first step up to 600 °C for 8 h under air at a rate of 1 °C per minute, cooled at a rate of 8 °C per minute, mixed again and then calcined at 900 °C for 7 h in air at a rate of 1 °C per minute. Finally, the solid was cooled at a rate of 8 °C per minute to room temperature.

Thermal analysis: Differential scanning calorimetry (DSC) and thermogravimetric analysis (TGA) were employed for the thermal characterization of the materials. Simultaneous TG-DTA curves were obtained using the TA Instruments Q600 system analyser. The measurements were carried out in a N_2 atmosphere with a flow rate of 100 mL min^{-1}. High-purity aluminium oxide was used as the reference material. The temperature was calibrated using the Curie nickel point as a reference. Samples weighing approximately 10 mg were placed in a high-purity alumina crucible. DSC and TGA were carried out in the temperature range from room temperature to 950 °C at a heating rate of 10 °C min^{-1}.

Structural characterization: The structural analysis was conducted by powder diffractometry (powder X-ray diffractometry, PXRD). The pulverised sample was pressed inside a sample holder to form a flat, smooth, and regular surface. A Rigaku SmartLab diffractometer with a theta:2-theta goniometer configuration was used to produce the diffractogram. The diffraction data were collected from 10^0 to 80^0 of 2θ at a scan rate of 2^0 2θ per minute.

Morphological characterization: For the morphological analysis, a Tescan VEGA3—LaB_6 scanning electron microscope coupled with an energy dispersive spectroscopy system (EDAX Element) for elemental microanalysis was used.

Electrochemical characterization: The electrochemical characterisation was carried out using a Maccor 4000 series cycler. Before characterisation, the powders were transformed into electrodes. To this end, about 0.3 g of the material was mixed with 0.045 g of carbon black (Super P, MMM Carbon, Brussels, Belgium). Then, 0.030 g of polytetrafluoroethylene (PTFE, Dupont, USA) was added, and the mixture was pounded in a mortar until the powders were all incorporated inside the PTFE. The percentages of components in the mixture were as follows: active material 80%, carbon black 12%, PTFE 8%. The mixture was then placed between two plastic sheets and calendared until it reached a final thickness of 70–110 μm. Circular electrodes of 12 mm in diameter were cut from the tape obtained, and their weight was evaluated. The electrodes were placed inside a coin cell and assembled with a 14 mm diameter lithium metal disk as counter electrode and a 16 mm diameter glass wool disk (Whatman Grade GF/A) as a separator. Lithium cells were filled with a 1M solution of $LiPF_6$ in ethylene carbonate/dimethyl carbonate 50/50 (*v*/*v*) (Aldrich LP30 battery grade).

The electrochemical test was carried out with a first charge cycle at 6 mA g^{-1} up to a potential of 4.8 V, followed by discharge and charge cycles at 30 mA g^{-1} of current. The end discharge voltage was set to 1.5 V. To evaluate the rate capability, the capacity at different discharge rates was also evaluated. In this case, the charge was conducted at 10 mA g^{-1}. The discharges were carried out, respectively, at 10, 20, 100, 200, 300, and 500 mA g^{-1}.

3. Results and Discussion

Thermal analysis: The synthesis of the materials occurred through a simple two-step process, as reported by Rapulenyane et al. [42]. The first step is needed to decompose the metal acetates, while the second step produces the sintering of the material. The acetates' decomposition temperature was evaluated by thermogravimetry. To eliminate the effect brought about by the loss of crystallisation water and highlight the thermal decomposition process of the acetates, the thermal analysis was carried out on the solid material obtained after the dissolution of the acetates in water and their subsequent evaporation. To this end, suitable stoichiometric quantities of the acetates were dissolved in distilled water. The solution was stirred at 1000 rpm at 100 °C until the complete evaporation of the solvent. The result of the analysis is shown in Figure 1.

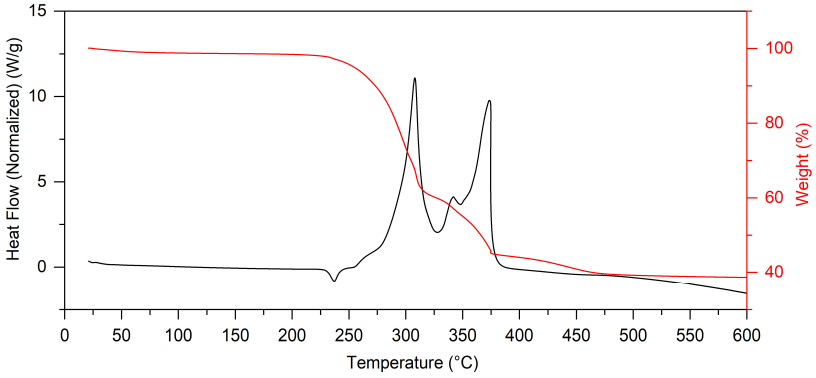

Figure 1. TGA and DTA curves of the solid material obtained after the dissolution of the lithium, manganese, and nickel acetates in water and their subsequent evaporation.

Up to 220 °C, no loss of weight is observed, confirming that the solvent was removed from the acetates. The decomposition process occurs in the range between 220 and 470 °C in three distinguishable steps. An interaction effect due to the intimate mixture of the components is expected, which does not allow for the straightforward assignment of the single decomposition step to a specific acetate. Moreover, the decomposition temperatures of the single phenomena are very similar, as in the case of the Mn and Ni acetates. Usually, the lattice water occurs at a temperature of around 250–300 °C, while the metal acetate decomposition is in the range of 300–450 °C. So, the first step of weight loss could be reasonably assigned to the loss of the lattice water of all the acetates, while the second step could be associated with the decomposition of both the Ni and Mg acetates, due to the comparable temperatures of the two processes. The last step could be due to the contribution of both the lithium degradation process and the nickel second-step decomposition. The DTA curve shows an exothermic peak for each step.

The total weight loss that occurs in this temperature range is about 40%, a percentage which roughly corresponds to the sum of the weight loss due to the decomposition of manganese, with the formation of both MnO_2 (Equation (1)) and Mn_2O_3 (Equation (2)), and lithium acetate, limited to the formation of Li_2CO_3 (Equation (3)).

$$2Mn(CH_3COO)_2 + 9O_2 \rightarrow 2MnO_2 + 8CO_2 + 6H_2O \quad (1)$$

$$4Mn(CH_3COO)_2 + 17O_2 \rightarrow 2Mn_2O_3 + 16CO_2 + 12H_2O \quad (2)$$

$$2Li(CH_3COO) + 4O_2 \rightarrow Li_2CO_3 + 3CO_2 + 3H_2O \quad (3)$$

What has been stated was confirmed regarding manganese acetate, whose thermal decomposition occurs at temperatures slightly above 300 °C [43], but not regarding lithium acetate, which has proven to be stable at temperatures up to 380 °C [44]. At this temperature, it decomposes, with the formation of Li_2CO_3 (Equation (3)). It is probable that the presence of the other metals decreases the temperature of decomposition of lithium acetate. A second thermal process is observed at temperatures higher than 320 °C, characterised by three peaks located at 350 °C, 375 °C, and 450 °C. The weight loss at the temperatures ranging from 320 to 480 °C is about 20%. This process could be related to the decomposition of the anhydrous nickel acetate that at 350 °C is converted into $NiCO_3$, releasing CO_2 into the gas phase (Equation (4)). The carbonate subsequently decomposes at 365 °C to give $NiO_{(s)}$, $CO_{2(g)}$, and $CO_{(g)}$ (Equation (5)) [45]. It is probable that, in this temperature range, the decomposition of Li_2CO_3 originating from lithium acetate is also completed (Equation (6)).

$$4Ni(CH_3COO)_2 + 8O_2 \rightarrow 2Ni_2CO_3 + 7CO_2 + 12H_2O \quad (4)$$

$$Ni_2CO_3 + O_2 \rightarrow Ni_2O_3 + CO_2 \quad (5)$$

$$Li_2CO_3 \rightarrow Li_2O + CO_2 \quad (6)$$

The decomposition of Li_2CO_3 should occur around 800 °C, but there is no evidence of this decomposition in the thermal analysis plot. As previously mentioned, it is also possible in this case that the presence of other metals could decrease the decomposition of Li_2CO_3 by moving it towards lower temperatures. Above 482 °C, there is no appreciable change in weight. The overall weight loss is 62%. The weight loss corresponds to the theorical weight loss related to the complete decomposition of the acetates (see Table 1). From the results of the thermal analysis, we decided to decompose the acetates at a temperature of 600 °C. The weight loss of lithium carbonate resulting from the decomposition of lithium acetate is also reported. The decomposition of manganese acetate is divided into two different columns, depending on whether the decomposition leads to the formation of manganese (IV) oxide or manganese (III) oxide.

Table 1. Percentage weight loss (based on anhydrous weight) during the decomposition of lithium, manganese, and nickel acetate.

Starting Compound	**$LiAc{\cdot}2H_2O$**	**Li_2CO_3**	**$Mn(Ac)_2{\cdot}4H_2O$**	**$Mn(Ac)_2{\cdot}4H_2O$**	**$Ni(Ac)_2{\cdot}4H_2O$**	**Total**
Final compound	Li_2CO_3	Li_2O	MnO_2	Mn_2O_3	Ni_2O_3	
Weight/g	3.060	-	2.451	1.225	1.244	7.980
Mol	0.030	0.015	0.010	0.005	0.005	0.065
Anhydrous weight/g	1.980	1.110	1.729	0.865	0.883	5.458
Weight final/g	1.110	0.450	0.869	0.395	0.413	2.128
Weight loss/% *	15.94	12.09	15.76	8.61	8.61	61.02

* Based on anhydrous weight.

Structural characterization: The LNMO can be considered as s solid solution with the formula $xLi_2MnO_3{\cdot}y(1-x)LiMnO_2{\cdot}(1-y)(1-x)LiNiO_2$ with x = 0.5 and y = 0.5. This structure includes the monoclinic Li_2MnO_3 (C2/m space group) and the rhombohedral $LiMnO_2$ and $LiNiO_2$ (R3m space group) phases [46]. Both the R3m and C2/m phases have a layered structure with a repeating transition metal layer, oxygen layer, and lithium layer. Figure 2 shows the XRDs of the samples prepared by the solid-state (SS) synthesis method and by the sol-gel (SG) procedure. Both samples show well-crystallised phases with sharp and intense peaks. The samples have essentially the same structure, which can be traced back to the trigonal one of the α-$NaFeO_2$ type belonging to space group R-3m (PDF card

no. 00-082-1495) [47]. α-$NaFeO_2$ has a layered structure where all octahedral sites are occupied by cations (i.e., Na^+ and Fe^{3+}), and layers of Na−O and Fe−O alternate along the lattice in the c-direction [48]. In our case, the good resolution of the peaks (006)/(012) and (108)/(110) shows that both materials have a well-organised layer structure [49]. The reflections between 20° and 23° in both materials are indicative of the presence of a C/2m superstructure derived from the Li_2MnO_3 component.

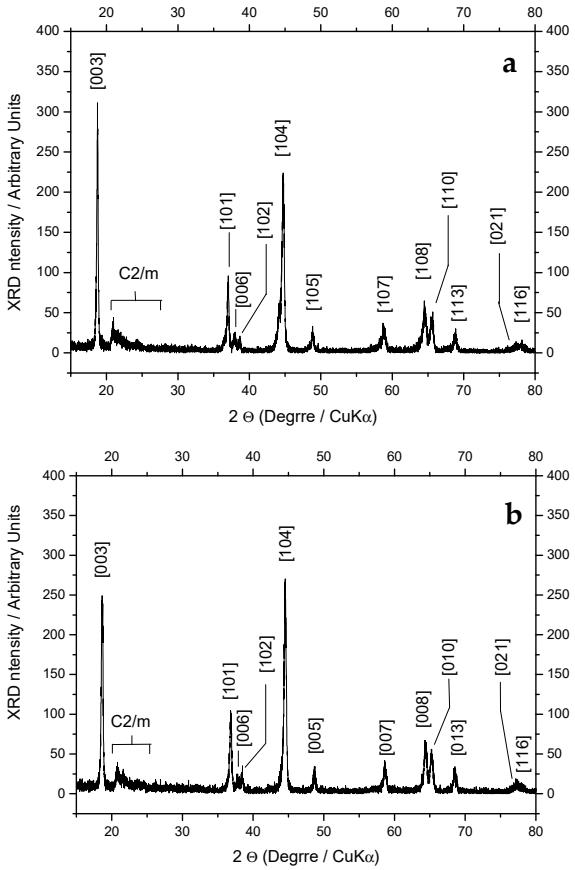

Figure 2. XRDs of the samples prepared by the solid-state synthesis method (**a**) and by the sol-gel procedure (**b**).

This superstructure indicates the presence of lithium ions within the layer occupied by the transition along the lattice in the c-direction [50]. The main difference between the two diffractograms lies in the intensity of the two reflection peaks [003] and [104]. In fact, while in the material prepared by SS reaction the intensity of peak [003] is higher than that of peak [104], the situation is reversed in the sample prepared by SG reaction. This difference reflects a different degree of Ni occupancy at the interlayer Li sites (cation mixing). In fact, since the ionic radius of Ni^{2+} (0.69 A) is similar in size to that of Li^+ (0.76 A), cation disorder can occur between Ni^{2+} and Li^+. To evaluate the cationic disorder, it is possible to refer to the factors R1 and R2 [51]. R1 represents the ratio between the intensity of the [003] and [104] peaks, while the factor R2 is defined as the ([006] + [102])/[101] intensity ratio. The higher the R1, the lower the amount of unwanted Li-Ni antisites [52]; the lower the R2, the better the hexagonal ordering [52]. Table 2 shows the values of the peak intensities and the R1 and R2 factors. From this analysis, the results show that the SS reaction not only inhibits cation disorder but also forms a better hexagonal layered structure, which boosts the stability of the internal structure. The material with a well-formed hexagonal layer structure and less Li^+/Ni^{2+} disorder is expected to present a better electrochemical performance [52]. A higher ionic order can facilitate the intercalation/deintercalation of Li

ions during the charge/discharge process, improving the electrochemical performance of the material.

Table 2. Intensities and their relative ratios of various peaks as calculated by XRD analysis.

Sample	I [003]	I [104]	I [006]	I [102]	I [101]	R1 = I [003]/I [104]	R2 = (I [006] + I [102])/I [101]
SS	311	224	17	17	87	1.39	0.39
SG	243	270	17	34	97	0.9	0.52

Morphological characterization: The surfaces of the samples were characterised by SEM. Figure 3 compares the micrographs (BSE mode) at low magnification (500×) which show the homogeneity of the powders obtained by the two synthesis methods, which are comparable and do not show areas of segregation of single elements. The inset pie charts show the result of the X-ray microanalysis performed on the samples. Considering the not-quantitative value of EDX, we can compare the two methods and affirm that they produce powders of similar composition and within the analytical error of X-ray spectroscopy. The theoretical percentages of the elements detected (excluding lithium) can be calculated using the following formula:

$$\% \, element(i) = 100 * \frac{CS_i * PM_i}{\sum CS_n * PM_n} \quad (7)$$

where CS_i and PM_i are, respectively, the stoichiometric coefficient and the molecular weight of the *ith* element. In the case of $Li_{1.2}Ni_{0.2}Mn_{0.6}O_2$, the percentages of the three constituent elements of the two samples are calculated to be 15.3% of nickel, 43.0% of manganese, and 41.7% of oxygen, values comparable to those obtained from the EDX estimate: 13.0% in the case of the SS method and 13.7% in the case of SG synthesis of nickel and 44.5% and 42.6% for manganese. Both materials are richer in oxygen (green slice) than the theoretical value, a probable effect of air exposure before the measurement.

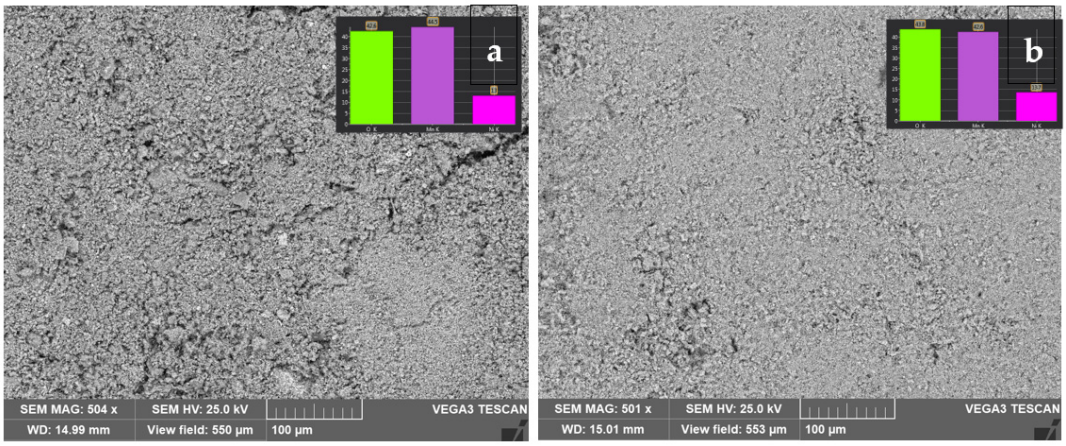

Figure 3. Low magnification BSE images (500×) of the material prepared by the solid-state synthesis method (**a**) and by the sol-gel procedure (**b**). The insets show the percentage composition of manganese (violet), nickel (pink), and oxygen (green) as evaluated by X-ray microanalysis.

Figure 4 compares the morphology of the powders at high magnifications (10 kx and 20 kx) for the material prepared by SS (on the left) or the SG method (on the right) to better point out microscopic differences. The two images in Figure 4a,b show two homogeneous areas of the two powders. We can appreciate the size and shape of the agglomerates and see that the SS method produces round, compact particles of micrometric dimensions while the SG procedure produces a less regular structure with larger and more compact aggregates surrounded by smaller, disorderly aggregated particles. Figure 4c,d show two areas that are less homogeneous at a lower magnification, which allows us to observe the presence

of bigger agglomerates in both powders. The larger structure in the material prepared by SS reaction shows a dimension of about 5 microns at its extremity and is shown at a larger magnification (20 kx, Figure 4e) to be lamellar and stratified with multiple layers superimposed on each other. On the other hand, its correspondent larger aggregates in the SG synthesis appear to be a compressed coalescence and fusion of smaller particles of submicrometric dimensions. At the same time, areas where structures resulting from the sintering of single particles persist can be observed.

Figure 4f clearly shows an enlargement of one of the SG agglomerated areas. Contrary to the SS material, the agglomerates appear smaller and do not have a lamellar organization but rather a compact and uniform structure. Overall, the material prepared with the SG method appears, although composed of two different morphological phases, more homogeneous, as particles and agglomerates are distributed in a more uniform way.

Electrochemical measurement: The electrochemical properties of the LNMO samples were evaluated by galvanostatic charge and discharge cycles. If we consider the total capacity provided by each of the two components of the LNMO, the theoretical specific capacity is 369 mAh g^{-1} (229 mAh g^{-1} for $0.5Li_2MnO_3$ + 140 mAh g^{-1} for $0.5LiNi_{0.5}Mn_{0.5}O_2$). This value corresponds exactly to the theoretical capacity calculated considering the complete extraction of lithium from the material (1.2 Li per formula unit $Li_{1.2}Ni_{0.2}Mn_{0.6}O_2$). Since this value is only theoretical, to avoid confusion, in the following, charge and discharge currents will be indicated as specific currents (and expressed in mA g^{-1}) and not as C-rate. Figure 5 shows the charge/discharge profiles of the first cycle between 1.5 and 4.8 V vs. Li^+/Li at a current density of 30 mA g^{-1}. The first region below 4.5 V is ascribed to the oxidation of Ni^{2+} to Ni^{4+}, while the subsequent flat region is assigned to the removal of Li_2O from such solid-solution materials.

The initial charge and discharge capacities for the sample prepared by the SS method were measured as 160 mAh g^{-1} and 80 mAh g^{-1}, respectively. After 25 cycles, the discharge capacity dropped to 60 mAh g^{-1}, which means that the layered structure of this material is not stable. The sample synthesised with the SG method provided the maximum initial discharge capacity of 87 mAh g^{-1}, which increased to 103 mAh g^{-1} in the second cycle and reached 108 mAh g^{-1} after 25 cycles. Both materials present a large first-cycle capacity hysteresis. This hysteresis is mainly due to the release of oxygen, which causes vacancy sites of oxide ions during the first charge; at high operating voltage (~4.8 V), the oxygen reacts rapidly with the electrolyte solvent (based on alkyl carbonates), forming decomposition products on the surface of the cathode and depositing inactive salts [53]. When used as the cathode in a full lithium-ion cell, the hysteresis could represent a serious problem. In fact, the low Coulombic efficiency causes harmful problems in the electrode balance [54]. Furthermore, only part of the lithium is reintroduced into the cathode, and this leads to the underutilization of the anodes.

The charging capacity exhibited by the material prepared via SG at the 25th cycle is higher than that exhibited at the 2nd cycle. In the final charging phase, there is a decrease in cell voltage, probably due to a parasitic phenomenon, with an increase in the charge capacity. Only part of this capacity is returned in the discharge, resulting in a little increase in discharge capacity in the 25th cycle compared to the 2nd. The voltage profile during charging recorded in the 25th cycle shows the onset of a plateau at 3.5 V that was absent in the 2nd cycle. Furthermore, the extent of this plateau is greater for the material prepared via the SS reaction than for the SG one. This decrease in voltage is usually explained through a phase transition mechanism from a layered to a spinel phase. This mechanism is due to increased extraction of Li^+ during charging to 4.8 V and the irreversible removal of Li and O. Both processes generate vacant sites where transition metal cations can migrate, resulting in the formation of the spinel phase [55–57]. This newly formed spinel phase can be subject to the Jahn–Teller distortion, the result of which is an increase in the ratio of Mn^{+3} to Mn^{+4}. After the phase transition, a disproportionate reaction can occur, producing Mn^{+4} and Mn^{+2}. The latter, being soluble in the electrolyte, can dissolve and cause a loss of active material [58]. This leads to fading of the capacity [59], as is mainly observed in the material

prepared by SS reaction. The formation of spinel phase domains is also responsible for the appearance of the plateau at 3.5 V due to the redox process involving the Mn^{+4}/Mn^{+3} couple [60].

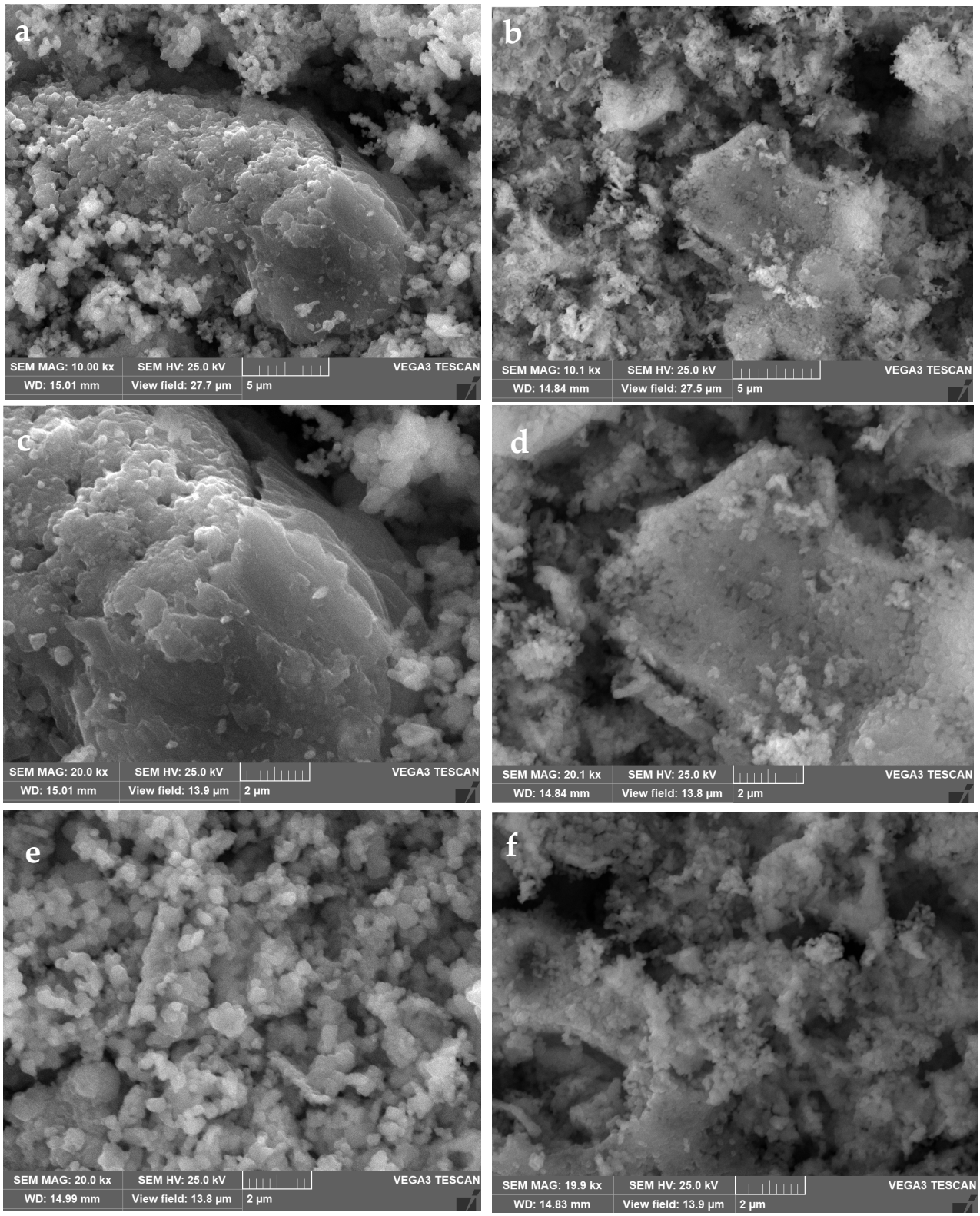

Figure 4. SEM images at various enlargements of the material prepared by the solid-state synthesis method (**a**,**c**,**e**) and by the sol-gel procedure (**b**,**d**,**f**).

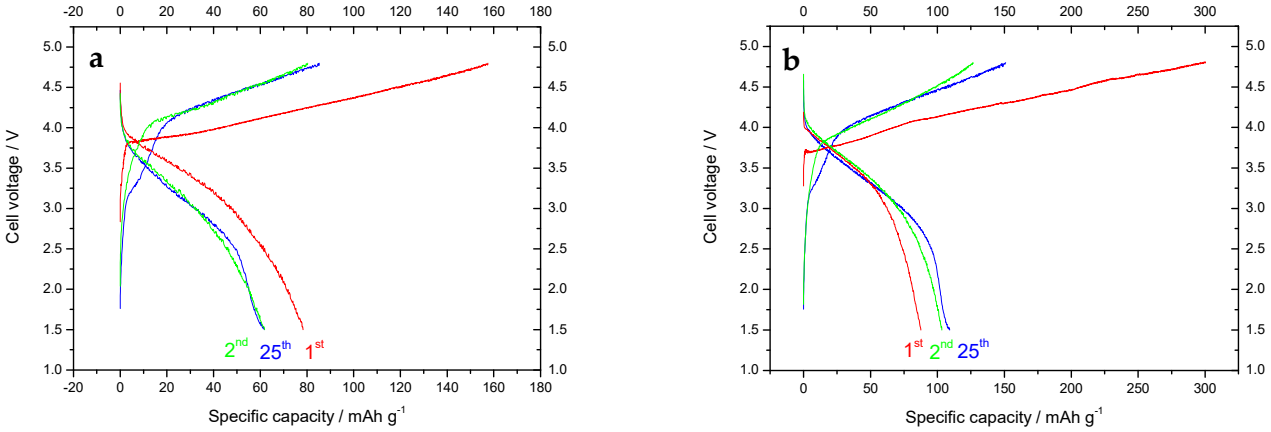

Figure 5. Voltage profiles recorded during the 1st, 2nd, and 25th cycles for the material prepared by the solid-state synthesis method (**a**) and by the sol-gel procedure (**b**).

The evolution of the capacity in the first 25 charge/discharge cycles and the charge coefficient are shown in Figure 6. The capacity in charge is always higher than in discharge. Consequently, the charge coefficient is always less than unity. This behaviour may be related to the fact that the transformation of Li_2MnO_3 is not complete in the first cycle and continues in the following cycles. In the sample produced by SS reaction, an increase in capacity is not observed with the progress of the number of cycles, which remains fixed at around 60 mAh g^{-1}, while a slight increase in capacity is observed for the sample produced using the SG technique, which reaches 108 mAh g^{-1} after 25 cycles. As cycling progresses, there is a decrease in the charge coefficient, probably due to a parasitic reaction involving the electrolyte solution, with loss of storage efficiency. The low efficiency found represents a serious problem for the practical applications of these materials. Further research must be carried out to limit the presence of parasitic phenomena that reduce efficiency. In general, the material prepared by SG exhibits substantially higher capacity than that prepared by SS synthesis. A further electrochemical characterization was carried out on the material prepared by SG to evaluate the capacity retention as the discharge speed varied. The material was therefore discharged at currents ranging from 10 to 500 mA g^{-1}. Charging was always carried out at a current of 10 mA g^{-1}. Figure 7a presents the discharge voltage profiles recorded for the material prepared by SG synthesis at different discharge currents.

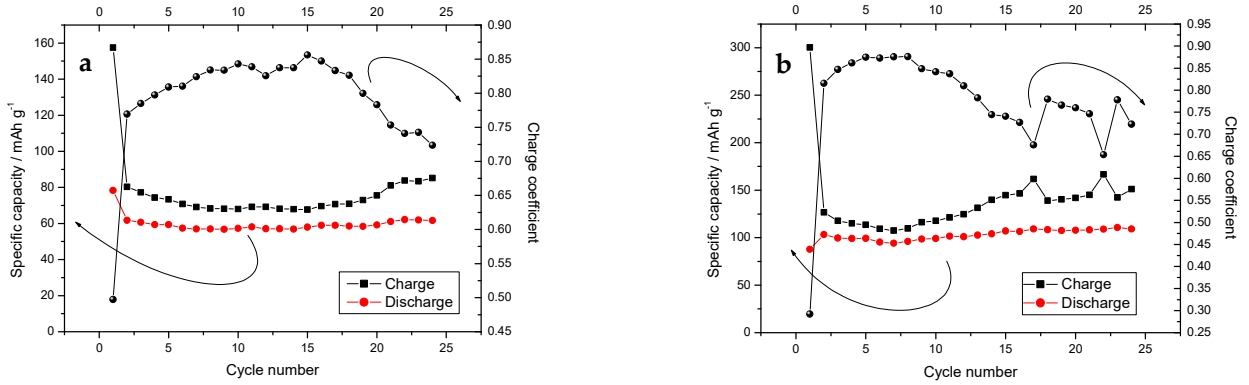

Figure 6. Specific capacity and charge coefficient as a function of the cycle number for the material prepared by the solid-state synthesis method (**a**) and by the sol-gel procedure (**b**).

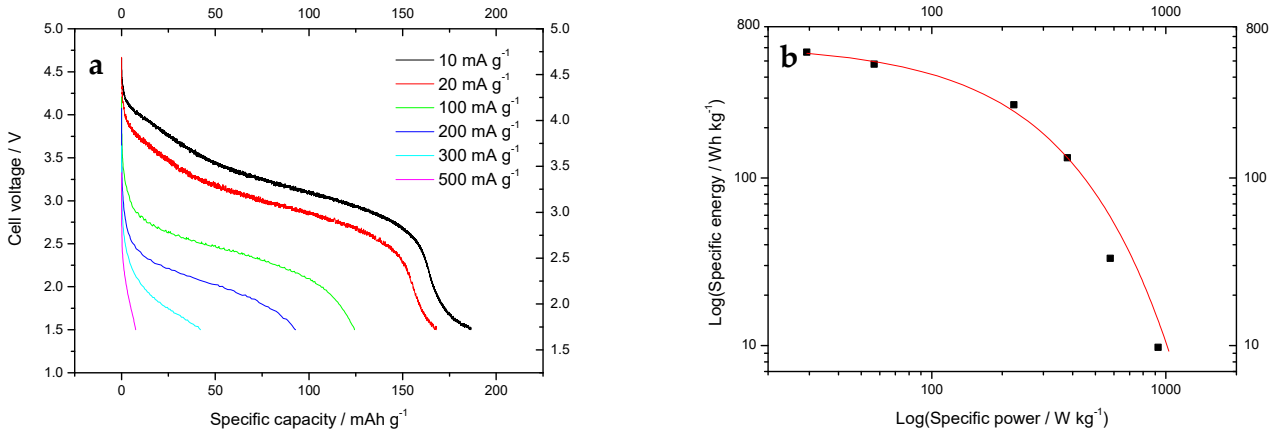

Figure 7. Voltage profiles recorded at various specific currents (**a**) and Ragone plot (**b**) for the material prepared by the sol-gel procedure. The specific current values are reported in the legend.

As the discharge current increases, there is a decrease in the specific capacity and, simultaneously, in the average discharge voltage. Both phenomena can be traced back to the slow diffusion of lithium inside the material, which determines a greater concentration of lithium on the surface of the material with a consequent decrease in voltage and early achievement of the end-of-discharge voltage. Performance at high discharge rates is very poor, probably due to the slow diffusion of lithium into the material. One possibility to reduce the energy barrier associated with lithium diffusion is to expand the spacing of the (003) planes without destroying the layered structure. In this way, it is possible to improve the diffusion kinetics of lithium. For this purpose, doping with small quantities of metals has proven to be very useful. For example, Sn-doped material exhibits an unexpected much-improved capacity above 3.0 V (vs. Li^+/Li) [61]. Although in the literature it is possible to find several sol-gel syntheses of LNMO, only a few of them use citric acid as a gelling agent. Furthermore, the synthetic method proposed in this paper does not involve the use of organic solvents, with a view to eco-designing the material. As already mentioned, the capacity of the LNMOs can be increased by using dopants, and the proposed SG method allowed us to obtain a material that showed better performance than LNMO material doped with tin [61].

At the lowest discharge rate (10 mA g^{-1}), the material exhibits a capacity of 186 mAh g^{-1} and an average discharge voltage of approximately 3.00 V, which corresponds to a specific energy of over 560 W kg^{-1}. At the highest discharge rate (500 mA g^{-1}), the material is still able to discharge just 13 mAh g^{-1} at an average voltage of 1.86 V, which corresponds to a specific power of over 920 W kg^{-1}. These results are summarised in Figure 7b, which reports the specific energy values at different values of the specific power delivered in the discharge (Ragone plot).

The capacity trend with increasing cycle number is shown in Figure 8. During 100 cycles, there was almost no capacity fading at low discharge rate, while a significant loss of capacity was observed for discharge currents higher than 200 mA g^{-1}.

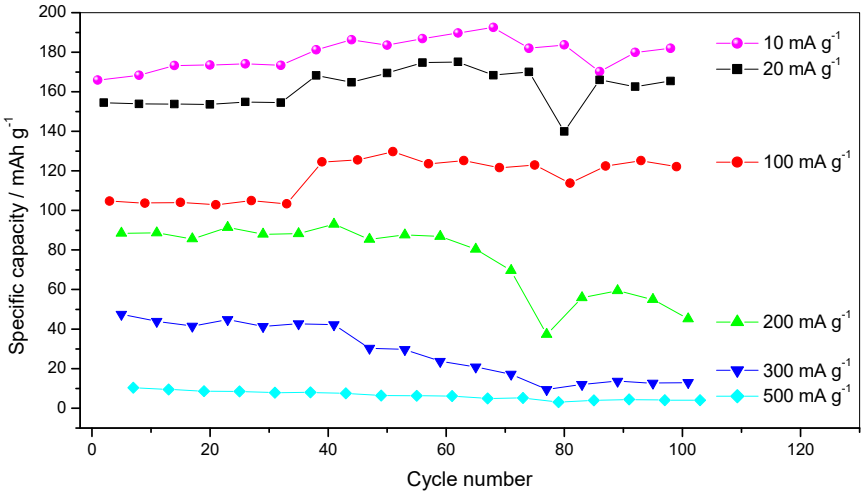

Figure 8. Specific capacity as a function of cycle number for the SG material recorded at different discharge rates.

4. Conclusions

In this work, the preparation of a lithium-rich cathode material was addressed through two simple and reliable synthesis methods, the solid-state and the sol-gel. Both methods involved a two-step thermal treatment, characterised by a first heating at 600 °C to decompose the acetates and a subsequent heating up to 900 °C to form the crystalline phase. The heat treatment was carried out at a well-determined heating rate to give rise to a reproducible synthesis process. The results showed that the sol-gel method produces a material which, at low discharge rates, has improved performance compared to that produced in the solid state. The sol-gel-prepared material was also tested at higher discharge rates and showed satisfactory performance.

Author Contributions: Conceptualization, P.P.P.; thermal analysis, A.A.; X-ray analysis, C.P.; SEM analysis, L.D.S.; writing—original draft preparation, P.P.P.; writing—review and editing, P.P.P., A.A., C.P. and L.D.S.; funding acquisition, P.P.P. All authors have read and agreed to the published version of the manuscript.

Funding: This research was funded by Ministry of Enterprises and Made in Italy, within the IPCEI project European Battery Innovation (EuBatIn).

Data Availability Statement: Data are available on request.

Conflicts of Interest: The authors declare no conflict of interest.

References

1. Nayak, P.K.; Erickson, E.M.; Schipper, F.; Penki, T.R.; Munichandraiah, N.; Adelhelm, P.; Sclar, H.; Amalraj, F.; Markovsky, B.; Aurbach, D. Review on challenges and recent advances in the electrochemical performance of high capacity Li- and Mn-rich cathode materials for Li-ion batteries. *Adv. Energy Mater.* **2018**, *8*, 1702397. [CrossRef]
2. Lu, Z.H.; MacNeil, D.D.; Dahn, J.R. Layered cathode materials $Li[Ni_xLi_{(1/3-2x/3)}Mn_{(2/3-x/3)}]O_2$ for lithium-ion batteries. *Electrochem. Solid. State Lett.* **2001**, *4*, A191–A194. [CrossRef]
3. Konishi, H.; Terada, S.; Okumura, T. Suppression of irreversible capacity for $Li_{1.16}Ni_{0.37}Mn_{0.47}O_2$ due to the chemical treatment with $(NH_4)_2SO_4$ in lithium-ion batteries. *J. Electroanal. Chem.* **2019**, *855*, 113492. [CrossRef]
4. Konishi, H.; Gunji, A.; Feng, X.; Furutsuki, S. Effect of transition metal composition on electrochemical performance of nickel-manganese-based lithium-rich layer-structured cathode materials in lithium-ion batteries. *J. Solid. State Chem.* **2017**, *249*, 80–86. [CrossRef]
5. Wang, G.; Xie, J.; Cao, G.; Zhu, T.; Zhao, X.; Zhang, S. Electrochemical performance of $0.5Li_2MnO_3$-$0.5LiNi_{0.5}Mn_{0.5}O_2$ nanotubes prepared by a self-templating route. *ECS Electrochem. Lett.* **2013**, *2*, A98–A101. [CrossRef]
6. Zhao, S.Q.; Guo, Z.Q.; Yan, K.; Wan, S.W.; He, F.R.; Sun, B.; Wang, G.X. Towards high-energy-density lithium-ion batteries: Strategies for developing high-capacity lithium-rich cathode materials. *Energy Storage Mater.* **2021**, *34*, 716–734. [CrossRef]
7. Zheng, J.M.; Gu, M.; Xiao, J.; Zuo, P.J.; Wang, C.M.; Zhang, J.G. Corrosion/fragmentation of layered composite cathode and related capacity/voltage fading during cycling process. *Nano Lett.* **2013**, *13*, 3824–3830. [CrossRef] [PubMed]

8. Chong, S.K.; Chen, Y.Z.; Yan, W.W.; Guo, S.W.; Tan, Q.; Wu, Y.F.; Jiang, T.; Liu, Y.N. Suppressing capacity fading and voltage decay of Li-rich layered cathode material by a surface nano-protective layer of CoF_2 for lithium-ion batteries. *J. Power Sources* **2016**, *332*, 230–239. [CrossRef]
9. Zhu, W.; Chong, S.K.; Sun, J.J.; Guo, S.W.; Tai, Z.G.; Wang, Y.J.; Liu, Y.N. The enhanced electrochemical performance of $Li_{1.2}Ni_{0.2}Mn_{0.6}O_2$ through coating MnF_2 nano protective layer. *Energy Technol.* **2019**, *7*, 1702397. [CrossRef]
10. Liu, Y.J.; Gao, Y.Y.; Wang, Q.L.; Dou, A.C. Influence of coated MnO_2 content on the electrochemical performance of $Li_{1.2}Ni_{0.2}Mn_{0.6}O_2$ cathodes. *Ionics* **2014**, *20*, 825–831. [CrossRef]
11. Mu, K.C.; Cao, Y.B.; Hu, G.R.; Du, K.; Yang, H.; Gan, Z.G.; Peng, Z.D. Enhanced electrochemical performance of Li-rich cathode $Li_{1.2}Ni_{0.2}Mn_{0.6}O_2$ by surface modification with WO_3 for lithium-ion batteries. *Electrochim. Acta* **2018**, *273*, 88–97. [CrossRef]
12. Zhao, Y.J.; Lv, Z.; Xu, T.; Li, J.X. SiO_2 coated $Li_{1.2}Ni_{0.2}Mn_{0.6}O_2$ as cathode materials with rate performance, HF scavenging and thermal properties for Li-ion batteries. *J. Alloys Compd.* **2017**, *715*, 105–111. [CrossRef]
13. Yan, P.F.; Zheng, J.M.; Zhang, X.F.; Xu, R.; Amine, K.; Xiao, J.; Zhang, J.G.; Wang, C.M. Atomic to nanoscale investigation of functionalities of an Al_2O_3 coating layer on a cathode for enhanced battery performance. *Chem. Mater.* **2016**, *28*, 857–863. [CrossRef]
14. Liu, Y.J.; Wang, Q.L.; Wang, X.Q.; Wang, T.C.; Gao, Y.Y.; Su, M.R.; Dou, A.C. Improved electrochemical performance of $Li_{1.2}Ni_{0.2}Mn_{0.6}O_2$ cathode material with fast ionic conductor Li_3VO_4 coating. *Ionics* **2015**, *21*, 2725–2733. [CrossRef]
15. Liu, Y.J.; Wang, Q.L.; Zhang, Z.Q.; Dou, A.C.; Pan, J.; Su, M.R. Investigation the electrochemical performance of layered cathode material $Li_{1.2}Ni_{0.2}Mn_{0.6}O_2$ coated with $Li_4Ti_5O_{12}$. Adv. *Powder Technol.* **2016**, *27*, 1481–1487. [CrossRef]
16. Zhang, L.L.; Chen, J.J.; Cheng, S.; Xiang, H.F. Enhanced electrochemical performances of $Li_{1.2}Ni_{0.2}Mn_{0.6}O_2$ cathode materials by coating $LiAlO_2$ for lithium-ion batteries. *Ceram. Int.* **2016**, *42*, 1870–1878. [CrossRef]
17. Sun, Y.; Zhang, X.; Cheng, J.; Guo, M.; Li, X.; Wang, C.; Sun, L.; Yan, J. Surface modification with lithium-ion conductor Li_3PO_4 to enhance the electrochemical performance of lithium-rich layered $Li_{1.2}Ni_{0.2}Mn_{0.6}O_2$. *Ionics* **2023**, *29*, 2141–2152. [CrossRef]
18. Liu, Y.; Liu, D.; Zhang, Z.; Zheng, S.; Wan, H.; Dou, A.C.; Su, M. Investigation of the structural and electrochemical performance of $Li_{1.2}Ni_{0.2}Mn_{0.6}O_2$ with Cr doping. *Ionics* **2017**, *24*, 2251–2259. [CrossRef]
19. Huang, Z.M.; Li, X.H.; Liang, Y.H.; He, Z.J. Structural and electrochemical characterization of Mg-doped $Li_{1.2}[Mn_{0.54}Ni_{0.13}Co_{0.13}]O_2$ cathode material for lithium ion batteries. *Solid. State Ion.* **2015**, *282*, 88–94. [CrossRef]
20. He, Z.J.; Wang, Z.X.; Chen, H.; Huang, Z.M. Electrochemical performance of zirconium doped lithium rich layered $Li_{1.2}Mn_{0.54}Ni_{0.13}Co_{0.13}O_2$ oxide with porous hollow structure. *J. Power Sources* **2015**, *299*, 334–341. [CrossRef]
21. Liu, H.; Tao, L.; Wang, W.; Zhang, B.; Su, M. Effects of raw materials on the electrochemical performance of Na-doped Li-rich cathode materials $Li[Li_{0.2}Ni_{0.2}Mn_{0.6}]O_2$. *Ionics* **2018**, *25*, 959–968. [CrossRef]
22. Yang, M.C.; Hu, B.; Geng, F.S.; Li, C.; Lou, X.B.; Hu, B.W. Mitigating voltage decay in high-capacity $Li_{1.2}Ni_{0.2}Mn_{0.6}O_2$ cathode material by surface K^+ doping. *Electrochim. Acta* **2018**, *291*, 278–286. [CrossRef]
23. Li, X.N.; Cao, Z.X.; Yue, H.Y.; Wang, Q.X.; Zhang, H.S.; Yang, S.T. Tuning primary particle growth of $Li_{1.2}Ni_{0.2}Mn_{0.6}O_2$ by Nd-modification for improving the electrochemical performance of lithium-ion batteries. *ACS Sustain. Chem. Eng.* **2019**, *7*, 5946–5952. [CrossRef]
24. He, T.; Chen, L.; Su, Y.; Lu, Y.; Bao, L.; Chen, G.; Zhang, Q.; Chen, S.; Wu, F. The effects of alkali metal ions with different ionic radii substituting in Li sites on the electrochemical properties of Ni-Rich cathode materials. *J. Power Sources* **2019**, *441*, 227195. [CrossRef]
25. Weber, D.; Tripković, D.; Kretschmer, K.; Bianchini, M.; Brezesinski, T. Surface Modification Strategies for Improving the Cycling. Performance of Ni-Rich. Cathode Materials. *Eur. J. Inorg. Chem.* **2020**, *33*, 3117–3130. [CrossRef]
26. Cai, Z.; Wang, S.; Zhu, H.; Tang, X.; Ma, Y.; Yu, D.Y.W.; Zhang, S.; Song, G.; Yang, W.; Xu, Y.; et al. Improvement of stability and capacity of Co-free, Li-rich layered oxide $Li_{1.2}Ni_{0.2}Mn_{0.6}O_2$ cathode material through defect control. *J. Colloid. Interface Sci. Part B* **2023**, *630*, 281–289. [CrossRef] [PubMed]
27. Xiang, Y.; Yin, Z.; Zhang, Y.; Li, X. Effects of synthesis conditions on the structural and electrochemical properties of the Li-rich material $Li[Li_{0.2}Ni_{0.17}Co_{0.16}Mn_{0.47}]O_2$ via the solid-state method. *Electrochim. Acta* **2013**, *91*, 214–218. [CrossRef]
28. Liu, J.; Chen, L.; Hou, M.; Wang, F.; Che, R.; Xia, Y. General synthesis of $xLi_2MnO_{3\cdot(1-x)}LiMn_{1/3}Ni_{1/3}Co_{1/3}O_2$ nanomaterials by a molten-salt method: Towards a high capacity and high power cathode for rechargeable lithium batteries. *J. Mater. Chem.* **2012**, *22*, 25380–25387. [CrossRef]
29. Fu, F.; Deng, Y.P.; Shen, C.H.; Xu, G.L.; Peng, X.X.; Wang, Q.; Xu, Y.F.; Fang, J.C.; Huang, L.; Sun, S.G. A hierarchical micro/nanostructured $0.5Li_2MnO_3\cdot0.5LiMn_{0.4}Ni_{0.3}Co_{0.3}O_2$ material synthesized by solvothermal route as high-rate cathode of lithium-ion battery. *Electrochem. Commun.* **2014**, *44*, 54–58. [CrossRef]
30. Zheng, F.; Ou, X.; Pan, Q.; Xiong, X.; Yang, C.; Liu, M. The effect of composite organic acid (citric acid & tartaric acid) on microstructure and electrochemical properties of $Li_{1.2}Mn_{0.54}Ni_{0.13}Co_{0.13}O_2$ Li-rich layered oxides. *J. Power Sources* **2017**, *346*, 31–39.
31. Zhong, Z.; Ye, N.; Wang, H.; Ma, Z. Low temperature combustion synthesis and performance of spherical $0.5Li_2MnLiNi_{0.5}Mn_{0.5}O_2$ cathode material for Li-ion batteries. *Chem. Eng. J.* **2011**, *175*, 579–584. [CrossRef]
32. Liu, Y.; Liu, D.; Wu, H.H.; Fan, X.; Dou, A.; Zhang, Q.; Su, M. Improved cycling stability of Na-doped cathode materials $Li_{1.2}Ni_{0.2}Mn_{0.6}O_2$ via a facile synthesis. *ACS Sustain. Chem. Eng.* **2018**, *6*, 13045–13055. [CrossRef]

33. Yang, P.; Li, H.; Wei, X.; Zhang, S.; Xing, Y. Structure tuned $Li_{1.2}Mn_{0.6}Ni_{0.2}O_2$ with low cation mixing and Ni segregation as high-performance cathode materials for Li-ion batteries. *Electrochim. Acta* **2018**, *271*, 276–283. [CrossRef]
34. Zhao, T.; Gao, X.; Wei, Z.; Guo, K.; Wu, F.; Li, L.; Chen, R. Three-dimensional $Li_{1.2}Ni_{0.2}Mn_{0.6}O_2$ cathode materials synthesized by a novel hydrothermal method for lithium-ion batteries. *J. Alloy. Compd.* **2018**, *757*, 16–23. [CrossRef]
35. Hao, R.; Liang, J.; Yang, Z.; Liang, C.; Cuan, X.; Gao, A.; Chen, H. Synthesis and Investigation of the nanocrystalline $Li_{1.2}Ni_{0.2}Mn_{0.6}O_2$ cathodes for Li-ion batteries by using ultrasonic/microwave-assisted co-precipitation method with different ultrasonic time. *J. S. China Norm. Univ.* **2017**, *49*, 6–10.
36. Li, L.; Wang, L.; Zhang, X.; Xue, Q.; Wei, L.; Wu, F.; Chen, R. 3D reticular $Li_{1.2}Ni_{0.2}Mn_{0.6}O_2$ cathode material for lithium-ion batteries. *ACS Appl. Mater. Interfaces* **2017**, *9*, 1516–1523. [CrossRef] [PubMed]
37. Wang, H.; Li, X.; Zhou, Q.; Ming, H.; Adkins, J.; Jin, L.; Jia, Z.; Fu, Y.; Zheng, J. Diversified $Li_{1.2}Ni_{0.2}Mn_{0.6}O_2$ nanoparticles from birnessite towards application specificity and enhancement in lithium-ion batteries. *J. Alloy. Compd.* **2014**, *604*, 217–225. [CrossRef]
38. Lim, J.H.; Bang, H.; Lee, K.S.; Amine, K.; Sun, Y.K. Electrochemical characterization of Li_2MnO_3– $Li[Ni_{1/3}Co_{1/3}Mn_{1/3}]O_2$–$LiNiO_2$ cathode synthesized via co-precipitation for lithium secondary batteries. *J. Power Sources* **2009**, *189*, 571–575. [CrossRef]
39. Hu, S.; Pillai, A.S.; Liang, G.; Pang, W.K.; Wang, H.; Li, Q.; Guo, Z. Li-rich layered oxides and their practical challenges: Recent progress and perspectives. *Electrochem. Energy Rev.* **2019**, *2*, 277–311. [CrossRef]
40. Jarvis, K.; Wang, C.C.; Manthiram, A.; Ferreira, P.J. The Role of Composition in the Atomic Structure, Oxygen Loss, and Capacity of Layered Li–Mn–Ni Oxide Cathodes. *J. Mater. Chem. A* **2014**, *2*, 1353–1362. [CrossRef]
41. Pechini, M.P. Method of Preparing Lead and Alkaline Earth Titanates and Niobates and Coating Method Using the Same to Form a Capacitor. US Patent No. 3,330,697, 11 July 1967.
42. Rapulenyane, N.; Ferg, E.; Luo, H. High-performance $Li_{1.2}Mn_{0.6}Ni_{0.2}O_2$ cathode materials prepared through a facile one-pot co-precipitation process for lithium-ion batteries. *J. Alloys Compd.* **2018**, *762*, 272–281. [CrossRef]
43. Afzal, M.; Butt, P.K.; Ahrnad, H. Kinetics of thermal decomposition of metal acetates. *J. Therm. Anal.* **1991**, *37*, 1015–1102. [CrossRef]
44. Tobón-Zapata, G.E.; Ferrer, E.G.; Etcheverry, S.B.; Baran, E.J. Thermal behaviour of pharmacology active lithium compounds. *J. Therm. Anal. Cal.* **2000**, *61*, 29–35. [CrossRef]
45. Hussein, G.A.M.; Nohman, A.K.H.; Attyia, K.M.A. Characterization of the decomposition course of nickel acetate tetrahydrate in air. *J. Therm. Anal.* **1994**, *42*, 1155–1165. [CrossRef]
46. Abdel-Ghany, A.; Hashem, A.M.; Mauger, A.; Julien, C.M. Lithium-Rich Cobalt-Free Manganese-Based Layered Cathode Materials for Li-Ion Batteries: Suppressing the Voltage Fading. *Energies* **2020**, *13*, 3487. [CrossRef]
47. Takeda, Y.; Akagi, J.; Edagawa, A.; Inagaki, M.; Naka, S. A preparation and polymorphic relations of sodium iron oxide ($NaFeO_2$). *Mater. Res. Bull.* **1980**, *15*, 1167–1172. [CrossRef]
48. Song, X.; Huang, H.; Zhong, W. Sucrose-assisted synthesis of layered lithium-rich oxide $Li[Li_{0.2}Mn_{0.56}Ni_{0.16}Co_{0.08}]O_2$ as a cathode of lithium-ion battery. *Crystals* **2019**, *9*, 436. [CrossRef]
49. Hamad, K.I.; Xing, Y. Stabilizing Li-rich NMC materials by using precursor salts with acetate and nitrate anions for Li-ion batteries. *Batteries* **2019**, *5*, 69. [CrossRef]
50. Lu, Z.; Beaulieu, L.Y.; Donaberger, R.A.; Thomas, R.A.; Dahn, J.R. Synthesis, structure, and electrochemical behavior of $Li[Ni_xLi_{1/3-2x/3}Mn_{2/3-x/3}]O_2$. *J. Electrochem. Soc.* **2002**, *149*, A778. [CrossRef]
51. Ohzuku, T.; Ueda, A.; Nagayama, M. Electrochemistry and structural chemistry of $LiNiO_2$ (R3m) for 4 volt secondary lithium cells. *J. Electrochem. Soc.* **1993**, *140*, 1862–1870. [CrossRef]
52. He, X.; Wang, J.; Wang, L.; Li, J. Nano-crystalline $Li_{1.2}Mn_{0.6}Ni_{0.2}O_2$ prepared via amorphous complex precursor and its electrochemical performances as cathode material for lithium-ion batteries. *Materials* **2016**, *9*, 661. [CrossRef] [PubMed]
53. Zhang, H.; Liu, H.; Piper, L.F.J.; Whittingham, M.S.; Zhou, G. Oxygen Loss in Layered Oxide Cathodes for Li-Ion Batteries: Mechanisms, Effects, and Mitigation. *Chem. Rev.* **2022**, *122*, 5641–5681. [CrossRef] [PubMed]
54. Parekh, M.-H.; Palanisamy, M.; Pol, V.G. Reserve lithium-ion batteries: Deciphering in situ lithiation of lithium-ion free vanadium pentoxide cathode with graphitic anode. *Carbon* **2023**, *203*, 561–570. [CrossRef]
55. Xie, H.X.; Cui, J.X.; Yao, Z.; Ding, X.K.; Zhang, Z.H.; Luo, D.; Lin, Z. Revealing the role of spinel phase on Li-rich layered oxides: A review. *Chem. Eng. J.* **2022**, *427*, 131978. [CrossRef]
56. Boulineau, A.; Simonin, L.; Colin, J.F.; Bourbon, C.; Patoux, S. First Evidence of Manganese-Nickel Segregation and Densification upon Cycling in Li-Rich Layered Oxides for Lithium Batteries. *Nano Lett.* **2013**, *13*, 3857–3863. [CrossRef] [PubMed]
57. Kim, D.; Sandi, G.; Croy, J.R.; Gallagher, K.G.; Kang, S.H.; Lee, E.; Slater, M.D.; Johnson, C.S.; Thackeray, M.M. Composite 'layered-layered-spinel' cathode structures for lithium-ion batteries. *J. Electrochem. Soc.* **2013**, *160*, A31–A38. [CrossRef]
58. Yang, Z.; Zheng, C.; Wei, Z.; Zhong, J.; Liu, H.; Feng, J.; Li, J.; Kang, F. Multi-dimensional correlation of layered Li-rich Mn-based cathode materials. *Energy Mater.* **2022**, *2*, 200006. [CrossRef]
59. Li, X.; Xu, Y.; Wang, C. Suppression of Jahn-Teller distortion of spinel $LiMn_2O_4$ cathode. *J. Alloys. Compd.* **2009**, *479*, 310–313. [CrossRef]

60. Wang, C.C.; Lin, Y.C.; Chou, P.H. Mitigation of layer to spinel conversion of a lithium-rich layered oxide cathode by substitution of Al in a lithium-ion battery. *RSC Adv.* **2015**, *5*, 68919–68928. [CrossRef]
61. Wang, Y.; Yang, Z.; Qian, Y.; Gu, L.; Zhou, H. New Insights into Improving Rate Performance of Lithium-Rich Cathode Material. *Adv. Mater.* **2015**, *27*, 3915–3920. [CrossRef]